Journal of Magnetism and Magnetic Materials 401 (2016) 173–179

Contents lists available at ScienceDirect

Journal of Magnetism and Magnetic Materials

journal homepage: www.elsevier.com/locate/jmmm

Magnetic and hyperfine properties of Fe_2P nanoparticles dispersed in a porous carbon matrix

G.L. Viali [a], G.R. Gonçalves [b], E.C. Passamani [a,*], J.C.C. Freitas [b], M.A. Schettino Jr. [b], A.Y. Takeuchi [a], C. Larica [a]

[a] Laboratory of Magnetometry and Mössbauer Effect, Department of Physics, Federal University of Espírito Santo, 29075-910 Vitória, ES, Brazil
[b] Laboratory of Carbon and Ceramic Materials, Department of Physics, Federal University of Espírito Santo, 29075-910 Vitória, ES, Brazil

ARTICLE INFO

Article history:
Received 18 June 2015
Received in revised form
2 October 2015
Accepted 9 October 2015

Keywords:
Mössbauer spectroscopy
Magnetic nanoparticles
Magnetic

ABSTRACT

Structural and magnetic properties of nanocomposite, consisting of Fe_2P particles dispersed in a porous carbon matrix, have fully been investigated using X-ray diffraction, Mössbauer and ac and dc magnetization measurements. Besides production of the nanocomposite, using an activated carbon (prepared by chemical activation of a char with H_3PO_4), impregnation with a Fe^{3+} salt in aqueous medium and subsequent heat treatments under N_2 flow, we found a formation of hexagonal $Fe_{2-x}P$ and orthorhombic FeP in a mass ratio of 4:1, respectively. Low temperature Mössbauer spectra revealed that a large fraction (ca. 28%) of the material is in the paramagnetic state, suggesting that part of the $Fe_{2-x}P$ phase appears in the form of very small particles. A metamagnetic phase transition was also observed for non-stoichiometric $Fe_{2-x}P$ nanoparticles. It is observed at about 150 K, well below the ordering temperature of the Fe_2P phase (230 K), and is dependent on the dc-probe fields. Also, the $Fe_{2-x}P$ nanoparticles were found to have a hard-like magnetic character at low temperatures, with coercive field H_C of 1.3 KOe. Considering these interesting magnetic and hyperfine properties and also the large specific surface area of the porous carbon matrix, which is not severely reduced after impregnation with the Fe-containing compounds, one may point to promising technological applications of the produced nanocomposite.

1. Introduction

The existence of size-dependent magnetic and catalytic properties in nanostructured materials has been extensively demonstrated in many studies [1–4]. Based on that, extensive efforts have been undertaken targeting the production of nanocatalysts, either non-supported ("free" particles) or supported in a specific matrix [5–8]. A class of materials that has systematically been studied from production as well as characterization viewpoints is that related to transition-metal (TM) compounds (e.g., oxides, carbides, nitrides, phosphides, etc.), since these TM-based products can catalyze many reactions [2,9–12], besides often presenting peculiar magnetic properties [1]. In particular, while the Ni_2P nanoproduct has been prepared by a wide variety of methods [13–18], the supported Fe_2P catalytic product has not received so far much attention as the previous one, mostly due to its poor activity in hydro-treating reactions [2]. Nevertheless, it was recently shown that the Fe_2P catalysts can favor NH_3 decomposition [19], enhancing the potential of this material for technological applicability. These observations have motivated the search for alternative methods for the production of free or supported Fe_2P nanoparticles. An example is a recent report on a novel carbothermal route for the synthesis of Fe_2P nanoparticles supported in carbon nanotubes [2]. Other investigated synthesis methods include the reaction of $Fe(CO)_5$ with alkyl phosphine [20] and the solid-state reaction between $FePO_4 \cdot 2H_2O$ and KBH_4 [8].

Concerning the Fe–P system, nearly non-stoichiometric $Fe_{2-x}P$ series has a hexagonal-type structure ($P\bar{6}2m$ space group) with lattice parameters close to $a=5.852$ Å and $c=3.453$ Å. Consequently, from the crystallographic viewpoint, it is difficult to distinguish the pure Fe_2P compound from the rest of the series. In the hexagonal-like structure, the Fe atoms occupy two non-equivalent sites named hereafter as Fe-I and Fe-II. The Fe-I atoms are located at the corners of a distorted tetrahedron of four P atoms, while the Fe-II atoms occupy a site with pyramidal-like symmetry formed with five P atoms [21]. On the other hand, from the magnetic viewpoint, the non-stoichiometric $Fe_{2-x}P$ series is very sensitive to the Fe-content [22,23]. Two important features should be addressed: (i) the paramagnetic-ferromagnetic (T_C=Curie temperature) transition temperature of the ordered Fe_2P compound is reported to be in the interval of 215–235 K (it depends on sample preparation conditions, i.e., different crystal quality: amount of

* Corresponding author.
E-mail address: edson@cce.ufes.br (E.C. Passamani).

http://dx.doi.org/10.1016/j.jmmm.2015.10.028
0304-8853/

impurities, of defects, etc) [22–25]; (ii) for Fe-content in the interval of $0.03 < x < 0.06$, the $Fe_{2-x}P$ series shows a metamagnetic phase transition (MPT), with a first-order character and T_C-values much smaller than those found in the stoichiometric phase, i.e., ca. 150 K [22,23]. These magnetic features can be used to characterize the Fe_2P phase embedded in a desired matrix (support) and consequently to improve their interest from basic as well as from technological viewpoints.

Here we report on the preparation and characterization (of structural, magnetic and hyperfine aspects) of a nanocomposite consisting of Fe_2P nanoparticles dispersed in a porous carbon support. The chosen support was an activated carbon (AC) prepared from the chemical activation (with H_3PO_4) of the endocarp of babassu coconut (scientific name: *Orbigny aphalerata Martius*). This lingocellulosic material is an abundant solid residue of the production of babassu oil in Brazil, presenting high lignin content and leading to the production of activated carbons with high porosity (mostly due to micro-pores) [26,27]. After chemical activation with H_3PO_4, a large amount of P-containing groups remain in the AC structure, mainly as phosphate [28]. In the method here described, the P-rich AC is impregnated with an aqueous solution of Fe^{3+} ions, leading to the production of nanostructured iron oxides embedded in the porous AC structure [29]. The reaction at temperatures in the range 700–900 °C of these iron oxides with the P-containing groups present in the AC results in the formation of Fe phosphate and, at even higher temperatures (1000 °C), these are reduced to Fe_2P and FeP species.

Following this method, we were able to prepare Fe_2P particles with crystallite sizes of ca. 80 nm embedded in a porous carbon matrix with an initial specific surface area (SSA) of about 2000 m^2/g, a feature that enhances the technological applicability of the produced nanocomposite in catalysis, for example. Moreover, since the $Fe_{2-x}P$ series has iron as one of its natural constituents, Mössbauer spectroscopy (MS) is the most suitable experimental method to determine hyperfine parameters (electron and spin densities at the Fe probe as well symmetry of the Fe-environment) and consequently to give information on the types and amounts of Fe phases present in the produced material. It is worth pointing out that despite the $Fe_{2-x}P$ compounds having similar crystallographic and hyperfine parameters, MS is capable of identify different Fe–P phases that are formed after heat treatments at high temperatures. Moreover, since the magnetic properties of the $Fe_{2-x}P$ series are sensitive to the Fe content, systematic magnetization measurements were performed, under applied magnetic fields and in a broad temperature range, in order to better characterize the material composition and their magnetic properties.

2. Experimental procedure

2.1. Preparation of samples

2.1.1. Production of the activated carbon (AC)

First, the endocarp of babassu coconut (EBC) was cut in small fiber-like fragments (with ~1 cm length) and impregnated with phosphoric acid (H_3PO_4), following a standard chemical activation procedure [28,30,31]. Approximately 200 g of the EBC precursor was inserted into a beaker together with 85% H_3PO_4 in a molar C:P of 1:2. A volume of water, covering completely the EBC and the H_3PO_4, was then added. This suspension was stirred during 24 h at room temperature (RT) and then dried at 110 °C for 12 h. The H_3PO_4-impregnated EBC powder was next submitted to a heat treatment at 700 °C during 1 h under a controlled N_2 gas flow. After cooling down to RT, the resulting product was repeatedly washed with distilled water under vacuum in a glove box until a neutral pH was obtained. The AC obtained by this method exhibited a specific surface area (SSA) of about 2000 m^2/g, determined using the BET method [32].

2.1.2. Synthesis of the nanocomposites

The AC-supported Fe-containing nanoparticles were obtained following a precipitation method [33], using iron nitrate [$Fe(NO_3)_3 \cdot 9H_2O$] as the iron source and ammonium hydroxide (NH_4OH) as the precipitating agent. First, 133 g of AC, 57.7 g of $Fe(NO_3)_3 \cdot 9H_2O$ and 250 mL of distilled water were mixed in a beaker; these amounts were chosen to give ca. 6 wt% of Fe in the nanocomposite. Next, an aqueous solution of NH_4OH (1.4 mol/L) was gradually added (~10 mL/min) and the mixture was stirred for a period of 24 h at RT, resulting in a gel-like product. The material was repeatedly washed with distilled water and filtered, until a neutral pH was obtained for the filtrate, and then it was dried for 2 h at 110 °C. This product was heat-treated under N_2 gas flow at a heating-rate of 5 °C/min at several temperatures from 700 up to 1000 °C, with a residence time of 2 h at each final temperature. The highest temperature (1000 °C) was chosen to stabilize the Fe–P compounds in the AC support, as shown below. The as-prepared nanocomposite is here referred to as Fe–P/AC and the products obtained after the heat treatments are named as Fe–P/AC-XX, where XX stands for the heat treatment temperature (in °C).

2.2. Characterization

The as-prepared material was analyzed by thermogravimetry (TG) and differential thermal analysis (DTA), using an apparatus from TA Instruments Model 6000; the experiments were conducted from RT to 1100 °C, with a heating-rate of 10 °C/min and a N_2 flow of 50 mL/min. The iron content in the nanocomposites was determined by atomic absorption spectrophotometry of Analytic Jena, operating at the mode of atomization of flame (the used resonance line was of 248.3 nm). The specific surface area of the samples was obtained by physisorption of N_2 at 77 K (Autosorb-1, Quantachrome Instruments), using the BET method with 11 points. The powders (with ca. 0.2 g) were purged under vacuum during 2–3 h at 200 °C previous to the beginning of the adsorption experiment. The nanocomposites were analyzed by powder X-ray diffraction (XRD), using a Shimadzu diffractometer, model XRD-6000, operating with Cu-K_α radiation ($\lambda = 1.5418$ Å) and equipped with a graphite diffracted-beam monochromator. The XRD patterns were collected at RT from 20° to 90° 2θ at a step of 0.5° and with 10 s per step. The XRD profile was fitted using the MAUD (Materials Analysis Using Diffraction) software (freeware) [34]. ^{57}Fe Mössbauer spectra were collected in a broad temperature range (from 15 to 300 K) in a Janis closed-cycle system, with the drive operating in constant acceleration transmission mode with a 50 mCi $^{57}Co/Rh$ matrix source. A spectrum of an α-Fe foil yields a linewidth of 0.29 mm/s when recorded in high velocity scale (~ ± 10 mm/s). The Mössbauer data were stored in a 512-channel MCS memory unit and numerically fitted using the NORMOS program [35], as will be discussed below. In Mössbauer experiments, the $^{57}Co/Rh$ source was kept at 300 K (RT), while the sample temperature was changed, which results in a second-order Doppler shift (SODS) effect in the Mössbauer spectra. The isomer shift (δ) values are quoted relative to metallic Fe at RT. Magnetic data were measured using a vibrating sample magnetometer (VSM) facility adapted in the Quantum Design/Evercool-II Physical Property Measurement System (PPMS). Magnetization versus temperature [$M(T)$] and magnetization versus applied field [M(H)] curves were recorded within a broad temperature interval (10–400 K) for different applied magnetic fields (H_{app}). Specifically, $M(T)$ curves were obtained using two different in-field protocols: field cooling (FC) and field heating (FH). In the FC-protocol, at

300 K, a magnetic field value is applied (probe-field) and the magnetization data are recorded while the sample is cooled down from 400 K to 10 K. Subsequently, the FH-protocol is proceeded and the M(T) data are obtained starting from the lowest temperature, while the sample is warmed up under the same probe-field. In general, a thermal hysteresis observed during the FC- and FH-protocols may be associated with first-order-type magnetic transitions, such as those found in non-stoichiometric $Fe_{2-x}P$ compounds caused by magnetoelastic effects [22,23]. Alternating current (ac) magnetic susceptibility (χ) experiments were also done using the PPMS setup over the same temperature interval. In these experiments, a static magnetic field (dc), with a magnitude in the range from 50 Oe up to 10 KOe, was applied in addition to the probe ac-field (with magnitude of 10 Oe and frequency of 1 or 10 KHz).

3. Results and discussions

We first show the properties of the composite materials obtained after different stages of heat treatment. In the sequence, we will discuss the magnetic and hyperfine characteristics of the Fe–P nanoparticles formed after annealing at 1000 °C under a N_2 gas flow. The Fe-content and the SSA of the as-prepared nanocomposite are equal to 5.7 wt% and 1600 m^2/g, respectively, evidencing that this is a highly porous material, presenting good dispersion of the Fe-containing species [29]. The TG and DTA curves recorded for the as-prepared material are shown in Fig. 1. After a strong initial weight loss around 100 °C, associated with the release of water adsorbed in the porous carbon support and also eventually bound to the synthesized iron oxides, a broad endothermic event is observed, starting at 300 °C and accompanied by a smooth weigh reduction. Then, a steep weight loss is detected just above 900 °C, matching a DTA endothermic peak at 950 °C. As it will be detailed below, these events are mainly attributed to the process of reduction of the iron oxides and iron phosphate, in agreement with previous findings on similar carbon-based nanocomposites containing nanostructured iron oxides [29].

Fig. 2(a) and (b) displays the XRD patterns and the Mössbauer spectra, respectively, of the as-prepared sample and of the nanocomposites obtained after heat treatments performed at 800 and 1000 °C (results of the samples annealed at temperatures close to 800 °C are similar to those present for the 800 °C sample). From Fig. 2(a), Bragg peaks are found at angular positions corresponding to the SiP_2O_7 compound in the XRD pattern of the as-prepared material, indicating the occurrence of a chemical reaction between

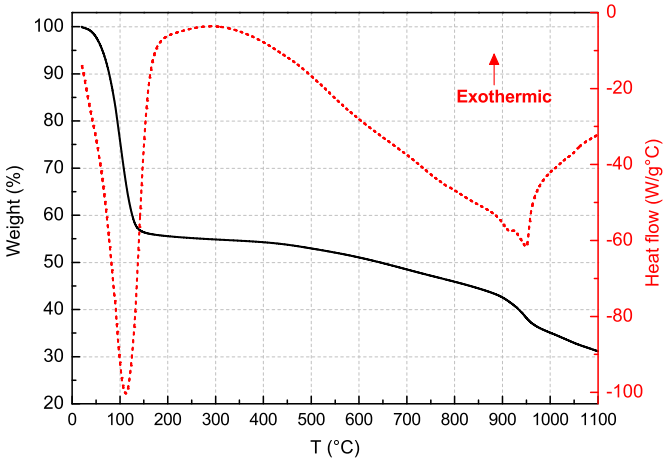

Fig. 1. TG and DTA curves recorded for the as-prepared material.

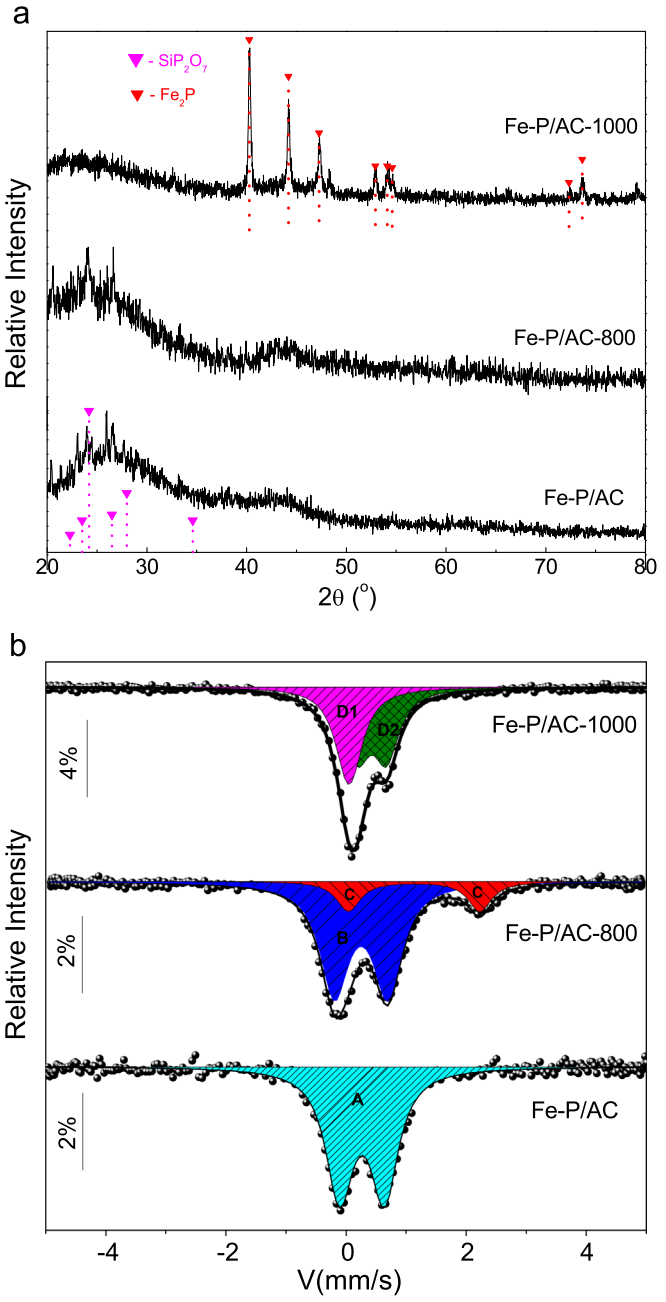

Fig. 2. Room temperature XRD patterns (a) and Mössbauer spectra (b) recorded for the as-prepared and heat-treated nanocomposites at the indicated temperatures. The components used to fit the Mössbauer spectra A, B, C, D1 and D2 are also shown in (b) with different colors.

the activating agent (H_3PO_4) and the Si-containing groups naturally present in the endocarp of babassu coconut [36]. The heat treatments performed up to 800 °C do not lead to substantial structural changes; the only noticeable feature is a slight narrowing of the peak at $2\theta \sim 43°$, which is (together with the peak at $2\theta \sim 25°$), associated with the turbostratic structure of the carbon matrix [37], pointing to a moderate carbon crystallite growth. It is worth mentioning that the main Bragg peaks, due to common Fe oxides, also appear in this angular range ($2\theta \sim 43°$) and thus the presence of nanocrystals of these oxides in the heat-treated nanocomposites cannot be disregarded [29,38].

When the as-prepared nanocomposite is heat-treated at 1000 °C in an oxygen-free atmosphere, a set of well-defined Bragg peaks emerges in the XRD pattern, as shown in Fig. 2(a). The

presence of these peaks indicates the formation of a new crystalline phase, as a consequence of thermal evolution and possible chemical reactions involving the Fe- and P-containing species present in the nanocomposites. Since the chemical activation with H_3PO_4 led to the production of a highly porous support, it can be inferred that the Fe–P phases are well dispersed within the pore network of the activated carbon matrix.

The RT Mössbauer spectra of the nanocomposites, shown in Fig. 2(b), suggest that all Fe-containing phases are in a paramagnetic or superparamagnetic (SPM) state. For the as-prepared nanocomposite, a doublet component (indicated as A in Fig. 2(b)), with hyperfine parameters typical of Fe^{+3}-oxides (δ=0.38 mm/s and quadrupole splitting (ΔQ)=0.74 mm/s), was used to fit its spectrum. The hyperfine parameters of the A-component suggest that initially the decomposition of the $Fe(NO_3)_3 \cdot 9H_2O$ compound leads to the formation of Fe_2O_3 nanoparticles, according to the hyperfine parameters reported in Ref. [39]. When the heat treatment temperature rises to equal and above 700 °C, two new paramagnetic RT contributions (B and C) appears in the spectra and their fractions enhance at the expense of the A-component. The B- and C-components have hyperfine parameters (δ^B =0.37 mm/s and ΔQ^B=0.92 mm/s and δ^C=1.1 mm/s and ΔQ^C =2.58 mm/s) close to those found in $FePO_4$ and $Fe_2P_2O_7$ compounds [40], respectively. The results observed for the C-component indicate a reduction process of the Fe^{+3}-phases as the temperature increases in an oxygen-free and carbon-rich environment. At 1000 °C, the spectrum is completely different from those obtained for samples annealed at lower temperatures. This spectrum is formed, at least, by two other paramagnetic components. In fact, it was fitted using the two known quadrupolar doublets (D1 and D2), originated from both iron sites of the Fe_2P crystal structure [Fe-I (pyramidal site) with δ=0.17 mm/s and ΔQ=0.10 mm/s and Fe-II (tetrahedral site) with δ=0.47 mm/s and ΔQ=0.50 mm/s] [24,41,42]. It is important to note that all (A, B, C, D1 and D2) components have their line widths broader ($\Gamma \sim$0.68 mm/s) than those expected for related crystalline phases [24,41,42]. Thus, this line broadening effect can indirectly be attributed to the nanoscale character of the Fe-containing phases in the nanocomposites, including the material heat-treated at the highest temperature (1000 °C). For this reason, a systematic characterization on the structural, hyperfine and magnetic properties of this nanocomposite (here referred to as Fe–P/AC-1000 sample) has been done and presented below.

Fig. 3 shows the fitted XRD pattern of the Fe–P/AC-1000 sample. Two crystalline Fe–P phases (Fe_2P and FeP compounds) were used in this fitting, as indicated in the figure. The fitting results allow us to estimate that 80% of the diffracting phases are associated with non-stoichiometric $Fe_{2-x}P$-like compounds, whereas 20% are due to the FeP phase. The calculated average crystallite size of the Fe_2P is about 80 nm, a value larger than that of 40 nm reported by Yao et al. for Fe_2P nanocrystals supported in carbon nanotubes [2]. A positive aspect about the Fe_2P-based nanocomposite (here described in terms of possible technological applications) is that the volume of $Fe_{2-x}P$ nanoparticles dispersed in the carbon support can easily be increased, by changing the amount of Fe salt used in the synthesis. Considering that the surface area of the support is still very high ($\sim$1600 m^2/g), there seems to be plenty of room for increasing the Fe loading in these nanocomposites, while keeping the high dispersion of the nanoparticles.

Temperature-dependent Mössbauer spectra of the Fe–P/AC-1000 sample are plotted in Fig. 4. As reported in the literature [24,41–46], for temperatures lower than T_C=230 K, the two Fe sites of the Fe_2P structure have different magnetic hyperfine fields (B_{hf}): B_{hf}^{Fe-I}=11.7 T and B_{hf}^{Fe-II}=18.1 T, for the pyramidal (Fe-I) and tetrahedral (Fe-II) sites, respectively. In addition, it is reported that

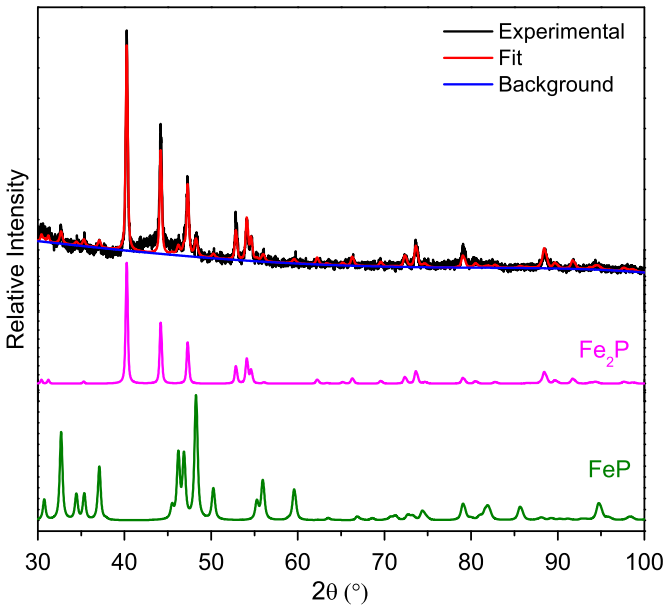

Fig. 3. XRD pattern of the Fe–P/AC-1000 sample and the fitting obtained considering a mixture of the hexagonal structure of the Fe_2P phase [22] and the orthorhombic structure of the FeP phase [41].

low temperature Mössbauer spectra of an Fe_2P single crystal exhibits reduced line width ($\Gamma \sim$0.32 mm/s) [42] and the presence of non-stoichiometric $Fe_{2-x}P$ contributions may change the spectra line shapes [46]. The 15 K-spectrum exhibited in Fig. 4 can only be fitted with four components (subspectra), whose hyperfine parameters are listed in Table 1. Two of these components are magnetically ordered subspectra with hyperfine parameters similar to those found in Fe_2P [24,41,42,44–46], except for their large Γ-values; these magnetic components are therefore associated with ordered $Fe_{2-x}P$ compounds. The other subspectra are two doublets, which suggest the occurrence of paramagnetic phases in the studied material, even at 15 K. Two possible models can be assumed to explain the existence of the doublets at 15 K: either the SPM effect of magnetically ordered $Fe_{2-x}P$ small particles and/or the presence of the FeP phase, also seen in the XRD data above discussed and commonly found when Fe–P systems are synthetized [41]. The following parameters of the doublets are obtained from the fitting of the 15 K-spectrum: δ=0.26 mm/s and ΔQ=0.30 mm/s and δ=0.47 mm/s and ΔQ=0.70 mm/s. Considering the SODS effect, which causes a shift of the spectrum to more positive velocities when the temperature is reduced [47], as clearly seen from the δ-values of the two magnetic subspectra displayed in Table 1, a pure attribution of these two doublets to the $Fe_{2-x}P$ compounds cannot fully describe our experimental data. Thus, we may also consider the presence of the FeP phase in agreement with the XRD data. However, the total fraction of these doublets is slightly larger (28% of Fe-containing phases) than the value obtained from the XRD data (20%). The apparent discrepancy in these fraction values could be an indication of the presence of SPM $Fe_{2-x}P$ phases even at temperatures as low as 15 K, contributing to the relative areas associated with the doublets in the Mössbauer spectra, but not distinguished in the XRD pattern (it basically increases the diffraction line associated with the $Fe_{2-x}P$ phases). In brief, the two broad doublets used to fit the RT Mössbauer spectrum of the Fe–P/AC-1000 sample are, in fact, due to Fe_2P as well as FeP phases, both in paramagnetic state at 300 K.

As the sample temperature increases, two effects can be noted from the Mössbauer spectra: (i) The B_{hf}-values of the Fe-I and Fe-II sites gradually reduce, as expected for conventional ferromagnets (see Table 1); (ii) The contribution associated with the

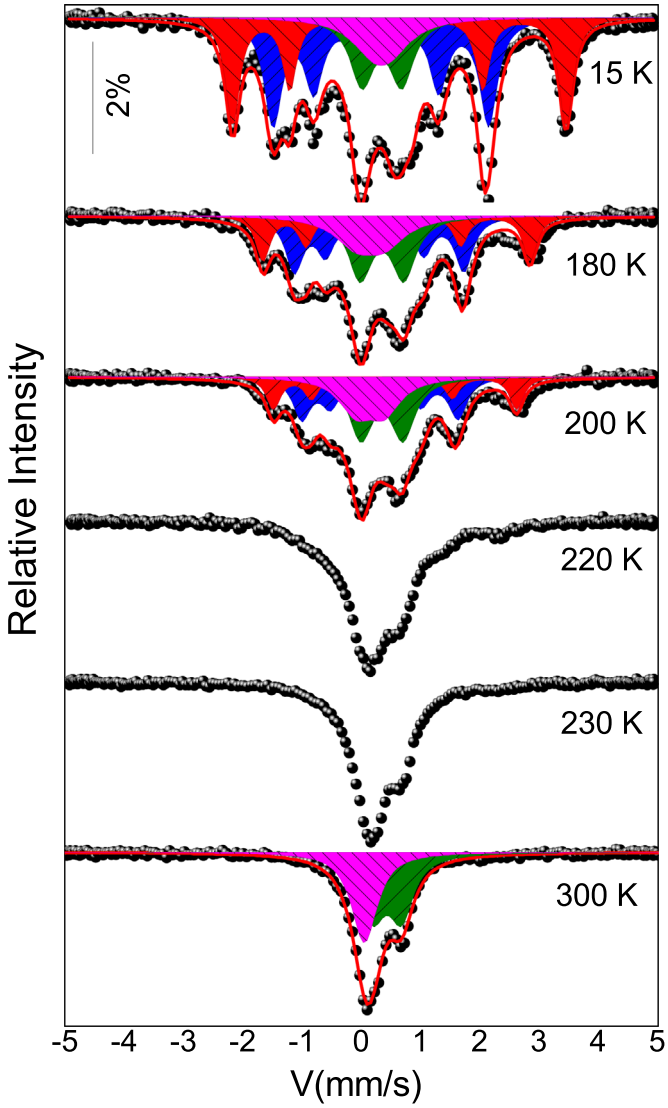

Fig. 4. Temperature-dependent Mössbauer spectra recorded for the Fe–P/AC-1000 sample. The components used to fit the spectra are also shown.

Table 1
Hyperfine parameters obtained from the fittings of the Mössbauer spectra shown in Fig. 4. The subspectra indicated with asterisks (*) are attributed to the Fe-I and Fe-II sites of the Fe_2P compound [34].

T (K)	Sites	δ (mm/s)[a]	ΔQ (mm/s)[b]	B_{hf} (T)[c]	RA (%)[d]
15	Fe_{-I}	0.26	0.3	–	12
	Fe_{-II}	0.47	0.7	–	16
	$^{*}Fe_{-I}$	0.41	–	11.7	40
	$^{*}Fe_{-II}$	0.66	–	18.1	32
180	Fe_{-I}	0.26	0.5	–	19
	Fe_{-II}	0.47	0.77	–	25
	$^{*}Fe_{-I}$	0.38	–	9.2	34
	$^{*}Fe_{-II}$	0.61	–	14.5	22
200	Fe_{-I}	0.26	0.5	–	22
	Fe_{-II}	0.47	0.74	–	29
	$^{*}Fe_{-I}$	0.38	–	8.5	30
	$^{*}Fe_{-II}$	0.61	–	13.2	19
300	Fe_{-I}	0.17	0.1	–	42
	Fe_{-II}	0.47	0.5	–	58

[a] δ: isomer shit.
[b] ΔQ: quadrupolar splitting.
[c] B_{hf}: magnetic hyperfine field.
[d] RA: relative area.

paramagnetic phases (RA – in Table 1) enhances, which is an experimental evidence that part of the $Fe_{2-x}P$ compounds is magnetically disordered below the T_C value (~230 K) of the pure Fe_2P compound [23,46]. Therefore, the fractions of the non-stoichiometric $Fe_{2-x}P$ and the pure Fe_2P compounds can now be estimated. In other words, at 180 K we would expect that the Fe_2P phase would be still magnetically ordered, but the fractions of the doublets have increased from 28% at 15 K to 44% at 180 K. Consequently, the increase of the doublets fraction with the temperature should be related to the paramagnetic character of non-stoichiometric $Fe_{2-x}P$ compounds and/or to the occurrence of SPM Fe_2P nanoparticles. Thus, from the temperature-dependent Mössbauer data, it can be inferred that the Fe–P-containing particles in the Fe–P/AC-1000 sample are formed by a broad distribution of magnetic ordering temperatures and/or particle sizes. It is important to note that the Mössbauer spectra recorded at 220 and 230 K (T_C of the Fe_2P compound) are not fitted due to the fact that magnetic and electric interactions are in the same order of magnitude. To fit these spectra, we would need to use a full Hamiltonian approach, which would not bring new features for the interpretation of these data, according to Ref. [44]. At 300 K, we recover the spectrum shown in Fig. 1(b), which was fitted with two broad doublets, now well characterized, i. e., these two broad doublets should be attributed to $Fe_{2-x}P$ and FeP phases with different particle sizes.

As mentioned above, non-stoichiometric $Fe_{2-x}P$ compounds have similar crystallographic and hyperfine properties when compared with the ordered Fe_2P phase [21,24,41,44], but they exhibit different magnetic behaviors. In principle, the non-stoichiometric $Fe_{2-x}P$ compounds have lower T_C and present a first-order-transition like feature at the interval $0.03 < x < 0.06$ [23]. Fig. 5 displays a set of results of magnetic characterization of the Fe–P/AC-1000 sample, performed with ac-probe and dc-bias field in a broad temperature range and with different frequencies (in the case of the ac-magnetic susceptibility data). The FC and FH $M(T)$ curves displayed in Fig. 5(a) show a thermal hysteresis in a temperature interval between 50 and 200 K, depending on the dc-probe field magnitude. At 10 kOe, this thermal hysteresis practically disappears; a result that is similar to that found in Ref. [23]. In fact, the presence of the thermal magnetic hysteresis in FC and FH protocols has frequently been found in non-stoichiometric $Fe_{2-x}P$ compounds [23,46]. In these systems, this effect is attributed to a MPT caused by a substantial change in c and a lattice parameters of the hexagonal structure at a defined temperature (magnetoelastic effects) [22,23,46]. Thus, the MPT can be modified by applied field [23,46] and by external pressure [46].

In particular, the MPT is observed in a relatively narrow temperature interval ($\Delta T = 1$ K) at about 214 K for a probe field of 5 Oe, for the $Fe_{1.998}P$ compound. However, we observed this $M(T)$ thermal hysteresis for FC and FH protocols in a broad temperature range, which may indicate the occurrence of a distribution of Fe_2P compounds with very different Fe contents and/or particle sizes; the latter is also known to strongly affect the temperature where the MPT occurs [48]. On the other hand, the $\chi(T)$ curves [Fig. 5(b)] present two peaks for zero and 50 Oe dc-applied magnetic field: a broad peak centered at about 150 K and a narrower one at 230 K. The lower temperature peak position (T_{max}) is weakly frequency sensitive, shifting to higher temperatures as the dc-bias field increases [Fig. 5(c)]. In the case of the higher temperature peak, the ac-probe field magnetic response is reduced as the dc-bias field increases, which may consistently indicate a critical ferromagnetic transition of the stoichiometric Fe_2P compound in large particles, according to its T_C-value reported in the literature [22,23]. The presence of the broad peak (T_{max}) at 150 K can be associated with the MPT of the $Fe_{2-x}P$ small particles, consistently with the $M(H)$ curves shown in Fig. 5(a).

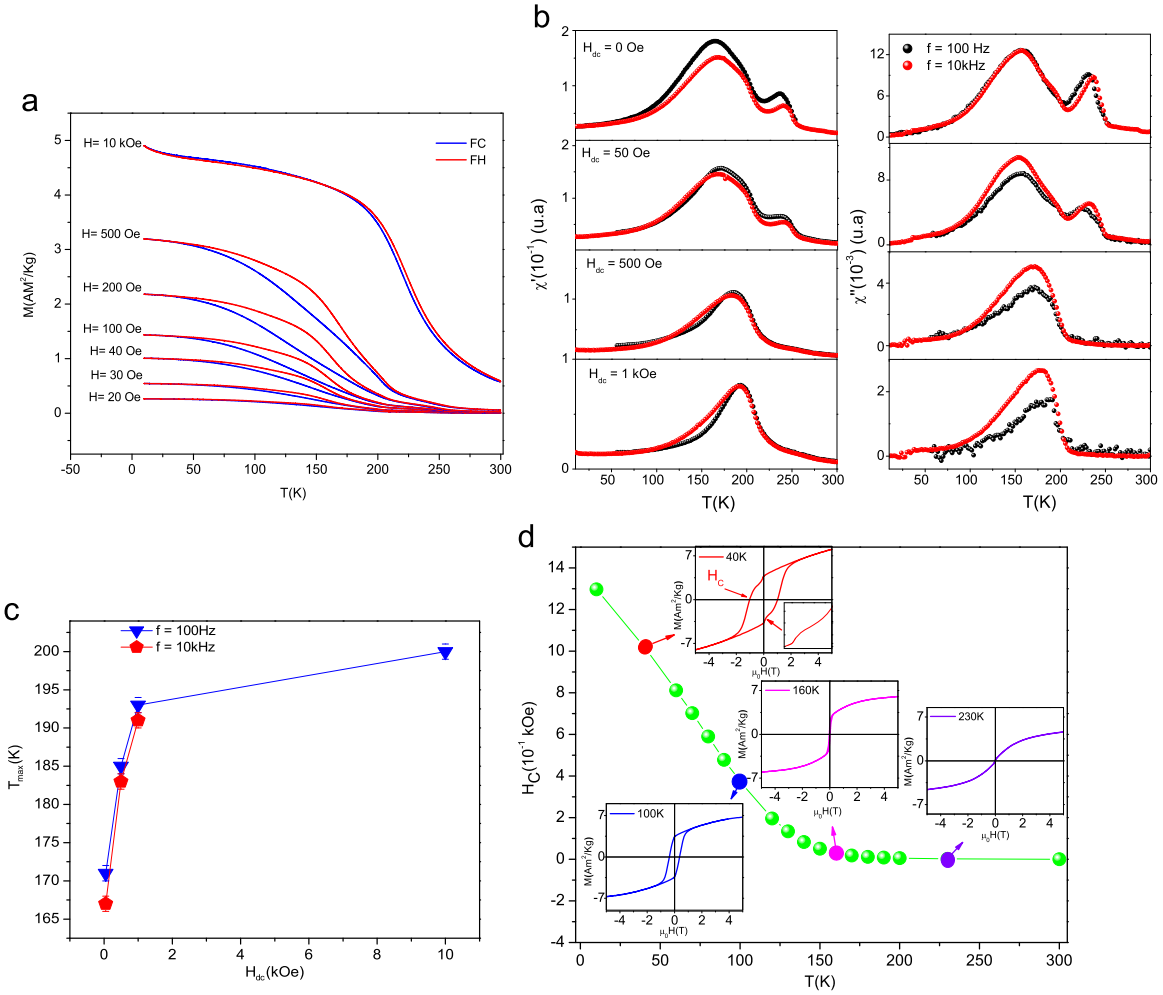

Fig. 5. Magnetic characterization of the Fe–P/AC-1000 sample.(a) FC and FH M(T) curves obtained for different dc-probe fields, as indicated; (b) temperature-dependent ac-magnetic susceptibility curves ($\chi(T)$) recorded with different frequencies and dc-probe fields; (c) behavior of the lower temperature peak of $\chi(T)$ as a function of the frequency and applied dc-fields and (d) temperature dependence of the coericve field (insets: $M(H)$ loops recorded with a scan field of ± 50 KOe).

Isothermal $M(H)$ loops, at some representative temperatures, are shown as insets of Fig. 5(d). For temperatures below 90 K, these loops present high coercive field (H_C) values, which is a typical behavior of nanocrystalline magnetic materials [49]. The non-saturation of magnetization in high fields (up to 50 KOe) and the large H_C-field are features that allow us to classify this nanocomposite as a hard magnet at low temperatures [50,51]. For this temperature range (< 90 K), it is also noticed a steep reduction of the magnetization for low field regions (near where the applied field direction is reversed). This effect, shown in the 40 K $M(H)$ loop [inset of Fig. 5(d)], is attributed to large particles of bulk FeP and Fe_2P, which are soft magnets [41,52]. As it can also be noted, above 180 K the H_C field value is nearly null, indicating that the bulk Fe_2P particles are magnetically soft ($Fe_{2-x}P$ phases are in paramagnetic state). It is important to emphasize that in the temperature range shown in Fig. 5(d) a paramagnetic contribution is always present, precluding the saturation of the magnetization. The non-stoichiometric $Fe_{2-x}P$ compounds in nanoscale are magnetically hard at low temperatures, a result not yet reported to the best of our knowledge.

4. Conclusion

We have been able to prepare magnetic nanoparticles of $Fe_{2-x}P$ compounds dispersed in an activated carbon support, which was produced by chemical activation starting from a natural lignocellulosic precursor (the endocarp of babassu coconut). The Fe-containing nanocomposites, composed by nanostructured iron oxides dispersed over the porous support, were synthesized by precipitation in aqueous medium. After heat treatments performed in non-oxidizing atmosphere up to 900 °C, the reaction between these iron oxides and the P-containing groups present in the activated carbon resulted in the formation of Fe phosphate and, at 1000 °C, these were reduced to Fe_2P (with varied stoichiometry) and FeP species. The nanocomposites were characterized using X-ray diffraction, Mössbauer spectroscopy and magnetization experiments performed in ac- and dc-modes. The magnetic nanocomposite, obtained after heat treatment at 1000 °C, was identified as composed by a mixture of $Fe_{2-x}P$ and FeP phases, with a broad distribution of particle sizes. By XRD, it was possible to estimate the fractions of the contributions due to $Fe_{2-x}P$ (80%) and FeP (20%) nanocrystalline phases (ratio of 4:1). From the magnetic viewpoint, 28% of the Fe-containing phases were found by Mössbauer spectroscopy to be paramagnetic at 15 K, suggesting that part of the $Fe_{2-x}P$ nanoparticles is SPM even at such a low temperature due to their small sizes. Also, the different magnetic features of the magnetically ordered and SPM $Fe_{2-x}P$ particles were shown up when we changed external parameters such as magnetic field, temperature and frequency of the ac-field. We have also shown that the synthesized nanoparticles exhibit a hard-like magnetic character. The magnetic nanocomposites were found to

present large porosity, with high dispersion of the Fe–P phases over the porous support, pointing to promising applications of these materials in the field of catalysis.

Acknowledgments

This work was supported by the following Brazilian agencies: CNPq, FAPES and CAPES.

References

[1] S.P. Gubin, Magnetic Nanoparticles, Wiley-VCH, Moscow, 2009.
[2] Z. Yao, H. Hai, Z. Lai, X. Zhang, F. Peng, C. Yan, Top. Catal. 55 (2012) 1040–1045.
[3] K.K. Haldar, S. Kundu, A. Patra, ACS Appl. Mater. Interfaces 6 (2014) 21946–21953.
[4] A.H. Lu, E.L. Salabas, F. Schüth, Angew. Chem. 46 (2007) 1222–1244.
[5] E. Muthuswamy, P.R. Kharel, G. Lawes, S.L. Brock, ACS Nano 3 (2009) 2383–2393.
[6] X. Huang, Q. Dong, H. Huang, L. Yue, Z. Zhu, J. Dai, J. Nanopart. Res. 16 (2014) 2785–2791.
[7] F. Luo, H.L. Su, W. Song, Z.M. Wang, Z.G. Yan, C.H. Yan, J. Mater. Chem. 14 (2004) 111–115.
[8] Y. Wang, Y. Wang, L. Zhang, H. Li, L. Jiao, H. Yuan, L. Chen, H. Tang, X. Yang, J. Power Sources 253 (2014) 360–365.
[9] Z.W. Yao, J. Alloy. Compd. 475 (2009) L38–L41.
[10] H.Y. Zhao, D. Li, P. Bui, S.T. Oyama, Appl. Catal. A: Gen. 391 (2011) 305–310.
[11] L. Song, S. Zhang, Q. Wei, J. Solid State Chem. 184 (2011) 1556–1560.
[12] S.L. Brock, S.C. Perera, K.L. Stamm, Eur. J. Chem. 10 (2004) 3364–3371.
[13] A. Wang, L. Ruan, Y. Teng, X. Li, M. Lu, J. Ren, Y. Wang, Y. Hu, J. Catal. 229 (2005) 314–321.
[14] P.A. Clark, S.T. Oyama, J. Catal. 218 (2003) 78–87.
[15] D.C. Phillips, S.J. Sawhill, R. Self, M.E. Bussell, J. Catal. 207 (2002) 266–273.
[16] S.J. Sawhill, D.C. Phillips, M.E. Bussell, J. Catal. 215 (2003) 208–219.
[17] L. Song, W. Li, G. Wang, M. Zhang, K. Tao, Catal. Today 125 (2007) 137–142.
[18] S. Yang, R. Prins, Chem. Commun. 33 (2005) 4178–4180.
[19] J. Donald, C. Xu, H. Hashimoto, E. Byambajav, Y. Ohtsuka, Appl. Catal. A: Gen. 375 (2010) 124–133.
[20] J. Park, B. Koo, K.Y. Yoon, Y. Hwang, M. Kang, J.G. Park, T. Hyeon, J. Am. Chem. Soc. 127 (2005) 8433–8440.
[21] S. Chiba, J. Phys. Soc. Jpn. 15 (1960) 581–585.
[22] H. Fujii, T. Hokabe, T. Kamigaichi, T. Okamoto, J. Phys. Soc. Jpn. 43 (1977) 41–46.
[23] L. Lundgren, G. Tarmohamed, O. Beckman, B. Carlsson, S. Rundqvist, Phys. Scr. 17 (1978) 39–48.
[24] M. Wautelet, A. Gérard, F. Grandjean, K. de Strooper, G. Robbrecht, Phys. Status Solidi 39 (1977) 425–430.
[25] A. Koumina, M. Bacmann, D. Fruchart, J.L. Soubeyroux, P. Wolfers, J. Tobola, S. Kaprzyk, S. Niziol, M. Mesnaoui, R. Zach, Ann. Chim. Sci. Des Mater. 23 (1998) 177–180.
[26] F.G. Emmerich, C.A. Luengo, Biomass Bioenergy 10 (1996) 41–44.
[27] E.F. Jaguaribe, L.L. Medeiros, M.C.S. Barreto, L.P. Araujo, Braz. J. Chem. Eng. 22 (2005) 41–47.
[28] A.M. Puziy, O.I. Poddubnaya, R.P. Socha, J. Gurgul, M. Wisniewski, Carbon 46 (2008) 2113–2123.
[29] M.A. Schettino, J.C.C. Freitas, M.K. Morigaki, E. Nunes, A.G. Cunha, E. C. Passamani, F.G. Emmerich, J. Nanopart. Res. 12 (2010) 3097–3103.
[30] J. Donald, Y. Ohtsuka, C.C. Xu, Mater. Lett. 65 (2011) 744–747.
[31] R. Fu, L. Liu, W. Huang, P. Sun, J. Appl. Polym. Sci. 87 (2003) 2253–2261.
[32] S. Brunauer, P.H. Emmett, E. Teller, J. Am. Chem. Soc. 60 (1938) 309–319.
[33] J. Schwarz, C. Contescu, A. Contescu, Chem. Rev. 95 (1995) 477–510.
[34] N. Benslim, S. Mehdaoui, O. Aissaoui, M. Benabdeslem, A. Bouasla, L. Bechiri, A. Otmani, X. Portier, J. Alloy. Compd. 489 (2010) 437–440.
[35] R.A. Brand, Laboratorium für Angewandte Physik, Universität Duisburg, Germany, 1992.
[36] J.C.C. Freitas, F.G. Emmerich, T.J. Bonagamba, Chem. Mater. 12 (2000) 711–718.
[37] Z.Q. Li, C.J. Lu, Z.P. Xia, Y. Zhou, Z. Luo, Carbon 45 (2007) 1686–1695.
[38] A. Martinez, Iron Oxides: Structure, Properties and Applications, Nova Science Publishers, New York, 2012.
[39] M. Cornell, U. Schwertmann, The Iron Oxides: Structure, Properties, Reactions, Occurrences and Uses, John Wiley, New York, 2006.
[40] M. Gadgil, K. Kulshreshtha, J. Solid State Chem. 111 (1994) 357–364.
[41] G.P. Felsher, F. Smith, Phys. Rev. B 3 (1971) 3046–3052.
[42] H. Kobayashi, J. Umemura, X.W. Zhang, Y. Uwatoko, J. Phys. Conf. Ser. 121 (2008) 032009–032013.
[43] J. Hubsch, G. Gavoille, J. Magn. Magn. Mater. 66 (1987) 17–22.
[44] T. Ericsson, L. Häggström, R. Wäppling, T. Methasiri, Phys. Scr. 21 (1980) 212–216.
[45] R.E. Bailey, J.F. Duncan, Inorg. Chem. 481 (1966) 1444–1447.
[46] H. Fujiwara, H. Kadomatsu, K. Tohma, H. Fujii, T. Okamoto, J. Magn. Magn. Mater. 21 (1980) 262–268.
[47] N.N. Greenwood, T.C. Gibb, Mossbauer Spectroscopy, Chapman and Hall, London, 1971.
[48] E.C. Passamani, V.P. Nascimento, C. Larica, A.Y. Takeuchi, A.L. Alves, J.R. Proveti, M.C. Pereira, J.D. Fabris, J. Alloy. Compd. 509 (2011) 7826–7832.
[49] E.C. Passamani, B.R. Segatto, C. Larica, R. Cohen, J.M. Greneche, J. Magn. Magn. Mater. 322 (2010) 3917–3925.
[50] E.C. Passamani, C. Larica, G. Viali, J.R. Andrez, A.Y. Takeuchi, V.P. Nascimento, V. A.P. Rodriguez, C.R. Ayala, E.B. Saitovitch, J. Alloy. Compd. 628 (2015) 164–169.
[51] R.A. McCurrie, Ferromagnetic Materials, Academic Press, London, 1994.
[52] L. Haggstrgm, A. Narayanasamy, J. Magn. Magn. Mater. 30 (1982) 249–256.